# Impedance Modeling and Stability Analysis of PV Grid-connected Inverter Systems Considering Frequency Coupling

Shaojian Song, *Member, IEEE*, Ze Wei, Yuzhang Lin, *Member, IEEE*, Bin Liu, and Hui Liu, *Senior Member, IEEE*

***Abstract*—Impedance analysis is an effective method to analyze the oscillation issue associated with grid-connected photovoltaic systems. However, the existing impedance modeling of a grid-connected photovoltaic inverter usually only considers the effect of a single perturbation frequency, ignoring the coupling frequency response between the internal control loops of a grid-connected inverter, which severely affects the accuracy of the stability analysis. Hence, a method of impedance modeling and stability analysis for grid-connected photovoltaic inverters considering cross-coupling frequency is proposed in this paper. First, the generation mechanism of frequency coupling in grid-connected photovoltaic inverters, and the relationship between the coupling frequency and perturbation frequency are analyzed. Secondly, a sequence impedance model of grid-connected photovoltaic systems considering the coupling frequency is established by using the harmonic linearization method. The impact of DC bus voltage control strategy on frequency coupling characteristics of a grid-connected photovoltaic system is evaluated, and the impact of a coupling frequency term on system stability is quantitatively analyzed. Finally, the advantages of the proposed method are verified by several simulations. The results show that the proposed impedance model can accurately predict the potential resonance points of the system, and the coupling frequency characteristics will become much stronger with smaller DC bus capacitance or larger bandwidth of the DC bus controller.**

***Index Terms*—DC bus voltage control, frequency coupling, grid-connected photovoltaic inverter system (PVs), harmonic linearization, sub-synchronous oscillation.**

## I. Introduction

RECENTLY, renewable energy resources such as photovoltaic and wind power generations have developed rapidly in China. Large-scale renewable energy resources are connected to the grid through power electronic conversion interfaces. The interactions among various grid-connected converters and interactions between converters and the power grid are prone to sub-/super synchronous oscillation/resonance (SSO/SSR) issues, which bring emerging severe challenges to the security and stability of the power grid [1]–[5], [38]–[40].

At present, the methods for analyzing the mechanism of this new type of SSO issue can be roughly divided into two categories: the time domain analysis method [6]–[9] and frequency domain analysis method [10]–[13]. Among them, the time domain analysis method can be further classified as the eigenvalue analysis method based on the state space model [6], [8] and the electromagnetic transient (EMT) simulation [7]–[9]. By developing the state space model of the system and analyzing its eigenvalues, the sub-/super synchronous dynamic characteristics of the system can be studied, and then the correctness of the theoretical analysis results can be further verified by EMT simulation. However, eigenvalue analysis has the following disadvantages [6], [8]: 1) it needs to integrate the photovoltaic or wind generation system models with the grid model. Even if the system changes slightly, the calculation and analysis of the model needs to be carried out repeatedly; 2) it requires the detailed structure and parameters of the system, which are usually hard to obtain in practice because of the technical confidentiality of the manufacturer. On the contrary, among the analysis methods in the frequency domain, the frequency scanning method and impedance analysis method have been proven to be two effective means to analyze the emerging SSO issue [10]–[12]. The impedance analysis method only needs to develop the impedance models of grid-connected inverters and AC grid respectively, and then the system stability can be analyzed by using the Nyquist criterion of the impedance ratio of the grid-connected inverter to the grid. Therefore, only the impedances of the changing parts needs to be recalculated, which will make the analysis much more efficient than the eigenvalue method. In addition, even when lacking the analytical impedance model of the system, the impedance model of the system can still be obtained by a frequency scanning experiment or simulation. In recent years, extensive research has been carried out in impedance modeling and stability analyzing for renewable energy generation systems. In [13]–[18], the existing modeling methods of distributed alternating current (AC) systems, such as reduced-order modeling of dynamic phasors (including amplitude and phase), modeling of the synchronous rotating frame (dq domain), directive reduced-order modeling, and modeling by harmonic linearization, are compared, and the advantages and limitations of these four methods are given. A method to model positive/negative sequence impedances

Manuscript received September 30, 2019; revised December 29, 2019; accepted January 14, 2020. Date of online publication February 13, 2020; date of current version February 28, 2020.

S. Song, Z. Wei, B. Liu and H. Liu are with the School of Electrical Engineering, Guangxi University, Guangxi 530004, China.

Y. Lin (corresponding author, e-mail: yuzhang_lin@uml.edu) is with the Department of Electrical and Computer Engineering, University of Massachusetts, Lowell, MA 01854 USA.

DOI: 10.17775/CSEEJPES.2019.02430

for grid-connected converters is presented based on harmonic linearization, and the stability criterion of grid-connected inverters based on impedance are proposed as well. In [19], the positive/negative sequence impedance models for three-phase grid-connected inverters with phase-locked loop (PLL) and digital control delay are established by the harmonic linearization and symmetrical component method. However, in the modeling for grid-connected converters, DC bus is usually regarded as an ideal voltage source, neglecting the impact of DC bus voltage control on the inverter output impedance, and ignoring the effects of frequency coupling between the AC side and DC side through the voltage source converter (VSC) [41]. In addition, the impacts of frequency coupling in grid-connected converters caused by the PLL control and asymmetric control of the d-axis and q-axis in the dq frame is overlooked, which makes the impedance model inaccurate, thus affecting the accuracy and even validity of stability analysis results [20]–[23].

The phenomenon of the coupling frequency in grid-connected inverters has attracted wide attention in academia [24], [25]. According to the research in [26], when SSO occurs in a photovoltaic system, both voltages and currents contain sub-synchronous (23.19 Hz) and super-synchronous (76.81 Hz) components. Reference [27] points out that the oscillation phenomenon caused by the interaction of the sub-synchronous frequency (2.5 Hz) and super-synchronous frequency (97.5 Hz) exists in the Type-III wind turbine. The two resonance frequencies in [26], [27] are exactly distributed on the right and left sides of the grid fundamental frequency (50 Hz), which are completely symmetrical. This phenomenon is called "mirror frequency" or "frequency coupling" [28]. A unified model for VSC with PLL and current control loop is developed by using a complex space vector and complex transfer function, and the mathematic relationship between the impedance models in the synchronous rotating frame (dq) and the stationary frame ($\alpha\beta$) is revealed as well [29]. In [30], a modified sequence-domain impedance definition and its equivalence to the dq-domain impedance definition for the stability analysis of AC power electronic systems are proposed, and a definition of a mirror-coupled system is presented. It is pointed out that the unreasonable PI parameters of a DC voltage controller and asymmetrical dq axis current control may result in frequency coupling. A systematic analysis method is proposed to explain the frequency coupling phenomenon, and it is pointed out that the locking angle of PLL is only related to the q-axis, which causes the unbalanced coupling frequency of three phase currents after the Park transformation of the current control loop [31]. References [30], [31] show that the unbalanced current control in the dq domain, PLL and DC voltage control can all produce frequency coupling. However, the analytical model for the frequency coupling characteristics of grid-connected inverters is not provided, without which it is impossible to quantitatively analyze the frequency coupling characteristics and their impact on the stability analysis of grid-connected inverters. Frequency-coupled admittance models of grid-connected inverters, doubly-fed wind generators (DFIG), modular-multilevel-converter high-voltage-direct-current (MMC-HVDC) systems, and other systems considering DC bus fluctuation are developed in [7], [16], [21], and [22], which filled the gap of the earlier literature [13]–[15], [17], [18]. The generalized Nyquist criterion is used in [7], [16], [21] and [22]. Although the stability of the system can be accurately evaluated, the potential resonance points of the system are hard to predict intuitively by coupling admittance models.

Currently, most research on frequency coupling characteristics are focusing on MMC-HVDCs, DFIGs, and permanent magnet synchronous generators (PMSG), and little work has been done to explore the frequency coupling characteristics of PVs, which are similar to PMSGs and DFIGs in circuit topology, as they are all equipped with VSCs which convert DC into AC. However, the front-end circuit operates in the maximum power point tracking (MPPT) mode in PVs for controlling its active power [32], and the latter is a rectifier circuit, which independently adopts double closed-loop controls (voltage outer loop and current inner loop) for its active and reactive power [33]. In addition, the output power of the PV array fluctuates dramatically due to the large variation of the irradiation intensity. It results in the fluctuation of DC bus voltage, and under such conditions, the DC side of VSC cannot be considered as an ideal voltage source anymore. Therefore, the frequency coupling characteristics of PVs should also be investigated.

Aiming to analyze the frequency coupling characteristics of PVs and evaluate their impacts on system stability, this paper develops the sequence impedance model with frequency coupling by harmonic linearization. The stability of PVs is then analyzed, and the effects on frequency coupling characteristics under the different capacitor sizes of DC buses are discussed as well. The main contributions of this paper are as follows:

1) The sequence impedance model of PVs, considering the frequency coupling between the AC and DC sides of the converter, is developed.

2) The impacts of DC bus capacitance and voltage controllers with MPPT on the frequency coupling characteristics of PVs are analyzed quantitatively.

3) An approach to predict the possible resonance points of PVs is presented by means of simulation scanning of the impedance model and the impedance-based Nyquist stability criterion.

## II. Analysis of Frequency Coupling Characteristics of PVs

In traditional small-signal impedance modeling, only the current response at the same frequency as the voltage perturbation is considered. In fact, when a voltage perturbation with a frequency of $f_{\mathrm{p}}$ is injected into the AC side of a grid-connected photovoltaic inverter at the point of common coupling (PCC), an AC current response with frequency of $f_{\mathrm{p}}$ is generated. At the same time, due to the feedback of the PLL and current control loop, a frequency coupling response is generated by convoluting the current signal with a frequency of $f_{\mathrm{p}}$ and the fundamental wave modulation signal in the pulse width modulation module. Similarly, a frequency coupling response

will also be generated on the AC side when a perturbation appears on the DC side capacitor. The frequency coupling effect is more significant, especially when the SSO occurs in the PVs. In this section, the generation mechanism and the frequency coupling relationship will be analyzed in detail.

### *A. Generation Mechanism of Frequency Coupling Characteristics of PVs*

The single-stage grid-connected photovoltaic generation system primarily includes a photovoltaic array, a DC capacitor, and a grid-connected inverter, as shown in Fig. 1. The three-phase voltages and currents at the PCC are denoted as $v_{\rm a}$, $v_{\rm b}, v_{\rm c}$, $i_{\rm a}$, $i_{\rm b}$, and $i_{\rm c}$ respectively. The terminal voltages of the three-phase inverter are denoted as $v_{\rm ta}$, $v_{\rm tb}$, and $v_{\rm tc}$ respectively, and the capacitor voltage of the DC bus is denoted as $v_{\rm dc}$. $L_{\rm p}$ is the filter inductance of the AC side, and $C_{\rm dc}$ is the DC capacitance. $\theta_{\rm PLL}$ is the phase angle of the grid voltage obtained by the PLL, and $Z_0$ is the grid impedance excluding the transformer.

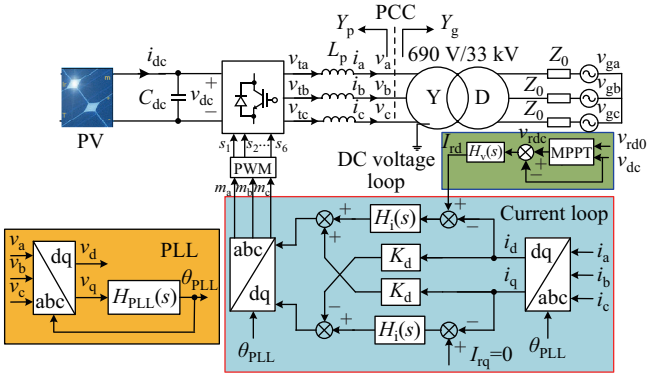


Fig. 1. Main circuit topology and control block diagram of the grid-connected photovoltaic inverter.

Because the power generations of photovoltaic arrays are greatly affected by solar irradiation and temperature, the input voltage of the VSC may fluctuate significantly. In order to mitigate the fluctuation of the DC bus voltage, a capacitor is usually installed at the back end of the photovoltaic arrays. In addition, the photovoltaic array has the current source output characteristic, so the grid-connected inverter can directly control the output voltage of the photovoltaic array, which does not need the intermediate DC-DC boost link. The single-stage grid-connected photovoltaic system combines MPPT control strategy with voltage control strategy to form the DC bus voltage loop control. It not only reduces the design cost and improves the conversion efficiency, but also simplifies the system structure and improves the system reliability [34].

The control strategy of the DC bus voltage is shown in the blue block in Fig. 1. MPPT tracks the maximum power point and outputs the corresponding voltage as the reference value. $I_{\rm rd}$ is obtained by the DC voltage controller after taking the difference between the actual DC bus voltage $v_{\rm dc}$ and the reference value. $I_{\rm rd}$ is superimposed to the input port of the current controller in the d axis so as to suppress the fluctuation of the DC bus voltage.

When there is no compensating current ($I_{\rm rd} = 0$) in the system, the current vector synthesized by the dq axis current is $I_1$. However, while the compensating current $I_{\rm rd}$ is not zero, the current vector synthesized by the dq axis current becomes $I_{\rm m}$, as shown in Fig. 2. According to the vector decomposition rule, the current vector $I_{\rm m}$ can be decomposed into vectors $I_{\rm m1}$ and $I_{\rm m2}$. The direction of $I_{\rm m1}$ is the same as that of $I_1$, and the direction of $I_{\rm m2}$ differs from that of $I_{\rm m1}$ by 90 degrees. $I_{\rm m2}$ can be called the "frequency coupling term." Therefore, the DC bus control strategy is one of the reasons for frequency coupling in PVs.

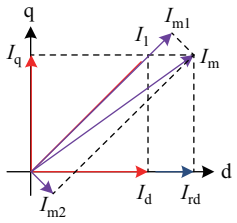


Fig. 2. Vector graph generated by frequency coupling.

Furthermore, the PLL control, and the asymmetric current control in the dq domain of the PVs can also cause the frequency coupling phenomenon. Its generation mechanisms have been analyzed in detail in [29]–[31], due to the limitation of space, it will not be discussed here.

### *B. Coupling Frequency Relationship of PVs*

When the PVs incorporate the PLL control, the asymmetric current control in the dq domain, and the voltage control of the DC bus, if a positive sequence voltage perturbation with a frequency of $f_{\rm p}$ is injected into the PCC as shown in Fig. 1, includes the positive current response with the same frequency as the voltage perturbation, and another negative sequence current response with frequency $f_{\rm p}-2f_1$ is generated simultaneously. This current is called a "coupling current" and the corresponding frequency $f_{\rm p}-2f_1$ is called a "coupling frequency." Conversely, if voltage perturbation is a negative sequence and its frequency is $f_{\rm n}$ (equal to $f_{\rm p}-2f_1$), the negative sequence current response with frequency $f_{\rm p}-2f_1$, a positive coupling current response with frequency $f_{\rm p}$ is also generated [35]. The frequency relationships of current responses caused by positive/negative sequence voltage perturbation are shown in Table I [36].

TABLE I
FREQUENCY RELATIONSHIP BETWEEN VOLTAGE PERTURBATIONS AND CURRENT RESPONSES

| Voltage perturbation frequency | Sequence | Current response frequency | Sequence |
|---|---|---|---|
| $f_{\rm p}$ | positive | $f_{\rm p}$ | positive |
| | | $f_{\rm n}-2f_1$ | negative |
| $f_{\rm n}$ | negative | $f_{\rm n}$ | negative |
| | | $f_{\rm n}+2f_1$ | positive |

## III. MODELING OF FREQUENCY COUPLING CHARACTERISTICS OF PVS

As frequency coupling characteristics are primarily related to the PLL control, the asymmetric current control in the

dq frame, and the DC bus voltage control, the modeling of frequency coupling characteristics are also primarily focusing on these three parts. In view of the fact that the parameters of the d-axis and q-axis current controllers in the dq domain are usually set to the same values, the parameters are symmetrical. Therefore, the effect of the asymmetric current control in the dq frame is neglected in the following impedance modeling of PVs.

### A. Average Model of Main Circuit

Based on Fig. 1, the time-domain average equation of the main circuit of the PVs can be established, as in (1) and (2):

$$L_{\mathrm{p}}\frac{\mathrm{d}}{\mathrm{d}t}\begin{bmatrix} i_{\mathrm{a}} \\ i_{\mathrm{b}} \\ i_{\mathrm{c}} \end{bmatrix} = k_{\mathrm{m}} v_{\mathrm{dc}} \begin{bmatrix} m_{\mathrm{a}} \\ m_{\mathrm{b}} \\ m_{\mathrm{c}} \end{bmatrix} - \begin{bmatrix} v_{\mathrm{a}} \\ v_{\mathrm{b}} \\ v_{\mathrm{c}} \end{bmatrix} \tag{1}$$

$$C_{\mathrm{dc}}\frac{\mathrm{d}v_{\mathrm{dc}}}{\mathrm{d}t} = i_{\mathrm{dc}} - k_{\mathrm{m}} v_{\mathrm{dc}}(m_{\mathrm{a}} i_{\mathrm{a}} + m_{\mathrm{b}} i_{\mathrm{b}} + m_{\mathrm{c}} i_{\mathrm{c}}) \tag{2}$$

where $L_{\mathrm{p}}$ is the filter inductor, $C_{\mathrm{dc}}$ is the DC bus capacitor, $m_{\mathrm{a}}$, $m_b$, and $m_{\mathrm{c}}$ are the modulation signals of the inverter, and $k_{\mathrm{m}}$ is the modulation gain.

Assuming that the phase-A voltage at PCC is superimposed with a positive voltage perturbation of the $f_{\mathrm{p}}$ frequency and a negative sequence voltage perturbation of the $f_{\mathrm{n}}$ frequency, the phase-A voltage and current can be expressed as follows:

$$\begin{aligned} v_{\mathrm{a}} = {} & V_1 \cos(2\pi f_1 t) + V_{\mathrm{p}} \cos(2\pi f_{\mathrm{p}} t + \varphi_{\mathrm{vp}}) \\ & + V_{\mathrm{n}} \cos(2\pi f_{\mathrm{n}} t + \varphi_{\mathrm{vn}}) \end{aligned} \tag{3}$$

$$\begin{aligned} i_{\mathrm{a}} = {} & I_1 \cos(2\pi f_1 t + \varphi_{\mathrm{i1}}) + I_{\mathrm{p}} \cos(2\pi f_{\mathrm{p}} t + \varphi_{\mathrm{ip}}) \\ & + I_{\mathrm{n}} \cos(2\pi f_{\mathrm{n}} t + \varphi_{\mathrm{in}}) \end{aligned} \tag{4}$$

where $V_1$ and $I_1$ are the amplitudes of the fundamental frequency voltage and current respectively; $V_{\mathrm{p}}$ and $V_{\mathrm{n}}$ are the amplitudes of the positive and negative sequence voltage perturbations, respectively; $I_{\mathrm{p}}$ and $I_{\mathrm{n}}$ are the amplitudes of the positive and negative sequence current responses, respectively; $\varphi_1$ is the phase of the fundamental frequency current response; and $\varphi_{\mathrm{p}}$ and $\varphi_{\mathrm{n}}$ are the phases of positive and negative sequence current responses, respectively.

In the frequency domain, the phase-A voltage and current with a small-signal perturbation can be written as follows:

$$V_{\mathrm{a}}[f] = \begin{cases} \boldsymbol{V}_1, & f = \pm f_1 \\ \boldsymbol{V}_{\mathrm{p}}, & f = \pm f_{\mathrm{p}} \\ \boldsymbol{V}_{\mathrm{n}}, & f = \pm f_{\mathrm{n}} \end{cases} \tag{5}$$

$$I_{\mathrm{a}}[f] = \begin{cases} \boldsymbol{I}_1, & f = \pm f_1 \\ \boldsymbol{I}_{\mathrm{p}}, & f = \pm f_{\mathrm{p}} \\ \boldsymbol{I}_{\mathrm{n}}, & f = \pm f_{\mathrm{n}} \end{cases} \tag{6}$$

where $\boldsymbol{V}_{\mathrm{p}} = (V_{\mathrm{p}}/2)\mathrm{e}^{\pm \mathrm{j}\varphi_{\mathrm{vp}}}$ and others follow the same notation.

As for AC systems, the following equivalence relationship exists between the positive sequence impedance and negative sequence impedance [35], as listed in (7).

$$Z_{\mathrm{p}}(s) = Z_{\mathrm{n}}^{*}(-s) \tag{7}$$

where $*$ denotes the conjugate. Then, in order to simplify the modeling process and pay more attention to the frequency coupling characteristics of PVs, we will only discuss the positive and negative sequence responses when the positive sequence voltage perturbation is injected into the PCC, and then develop the small-signal impedance model of the positive sequence subsystem. The impedance model for negative subsystems can be easily obtained from (7).

### B. Impedance Modeling of the Control Loop

#### 1) Small-signal Modeling of the DC Voltage Loop

In traditional modeling, the DC bus is usually regarded as an ideal voltage source, which ignores the effects of frequency coupling between the AC side and DC side through VSC. However, the dynamic time domain simulation indicates that when the AC side converter adopts DC voltage control, the DC voltage control interacts with the loop of the PLL control and current control, and then affects system stability. Thus, this section focuses on the modeling of the DC voltage loop.

Combining (1) and (2), the frequency-domain equation of the DC voltage can be written as follows:

$$V_{\mathrm{dc}}[\pm(f_{\mathrm{p}} - f_1)] = \frac{3[(sL_{\mathrm{p}} I_1^{*} + V_1) I_{\mathrm{p}} + I_1^{*} V_{\mathrm{p}}]}{2(I_{\mathrm{dc}} - sC_{\mathrm{dc}} V_{\mathrm{rd0}})} \tag{8}$$

where $V_{\mathrm{rd0}}$ is the reference value of the DC voltage, $I_1^{*}$ is the conjugate of the fundamental current.

From Fig. 1, it can be determined that because the existence of the MPPT control strategy in the front of the DC voltage loop, the influence of MPPT on the DC voltage loop modeling needs to be considered. The common algorithms of MPPT include the constant voltage method, conductance increment method, disturbance observation method, etc. [37]. Reference [37] points out that there is a linear relationship between the maximum power output voltage $v_{\mathrm{rd0}}$ and the open circuit voltage $U_{\mathrm{OC}}$ of the photovoltaic array. This relationship is not affected by the change of solar irradiation and temperature. The constant voltage method is based on this relationship. The linear relationship is $v_{\mathrm{rd0}} = 0.76\ U_{\mathrm{OC}}$. According to this expression, the MPPT control strategy based on the constant voltage method can be equivalent to a PI control, as shown in Fig. 3.

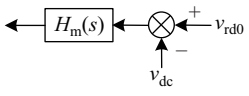


Fig. 3. Control block diagram of MPPT.

Thus the d-axis current reference $I_{\mathrm{rd}}$ can be obtained as follows:

$$I_{\mathrm{rd}}[\pm(f_{\mathrm{p}} - f_1)] = H_{\mathrm{v}}(s)(H_{\mathrm{m}}(s) - 1) V_{\mathrm{dc}}[\pm(f_{\mathrm{p}} - f_1)] \tag{9}$$

where $H_{\mathrm{v}}(s)$ is the transfer function of the voltage controller, and $H_{\mathrm{m}}(s)$ is the transfer function of the MPPT controller.

#### 2) Small-Signal Modeling of PLL

When a voltage perturbation exists at PCC, the phase from PLL contains not only the base frequency angle of $\theta_1$, but also

the angle deviation $\Delta\theta$ caused by the voltage perturbation. Thus, the output phase of PLL can be written as follows:

$$\theta_{\mathrm{PLL}}(t) = \theta_1 + \Delta\theta(t) \tag{10}$$

where $\theta_1 = 2\pi f_1$. Then, the linearization for PLL can be carried out to obtain the relationships between the perturbation voltage and the resulting angle deviation.

$$\Delta\theta[\pm(f_\mathrm{p} - f_1)] = G_\mathrm{p}(s)V_\mathrm{p} \tag{11}$$

$$G_\mathrm{p}(s) = \mp\mathrm{j}\frac{H_{\mathrm{PLL}}(s)}{1 + V_1 H_{\mathrm{PLL}}(s)} \tag{12}$$

where $H_{\mathrm{PLL}}(s)$ is the transfer function of the PLL.

*3) Small Signal Modeling of the Current Loop*

From Fig. 1, in order to obtain the d-axis and q-axis components of the currents in the frequency domain, three-phase currents are first transformed to the dq frame through the Park transformation, then the Fourier transform is conducted to obtain the dq components in the frequency domain:

$$I_\mathrm{d}[f] = \begin{cases} I_1\cos\varphi_{\mathrm{i}1}, & f = \mathrm{dc} \\ I_1\sin\varphi_{\mathrm{i}1}G_\mathrm{p}(s)V_\mathrm{p}[f] + I_\mathrm{p}[f], & f = \pm(f_\mathrm{p} - f_1) \end{cases} \tag{13}$$

$$I_\mathrm{q}[f] = \begin{cases} I_1\sin\varphi_{\mathrm{i}1}, & f = \mathrm{dc} \\ \mp\mathrm{j}I_\mathrm{p}[f] - I_1\cos\varphi_{\mathrm{i}1}G_\mathrm{p}(s)V_\mathrm{p}[f], & f = \pm(f_\mathrm{p} - f_1) \end{cases} \tag{14}$$

where $I_\mathrm{d}[f]$ and $I_\mathrm{q}[f]$ are the d-axis current and q-axis current in the frequency domain, respectively. Thus, according to the current control loop in Fig. 1, the output modulating signals of phase A can be written as follows:

$$\begin{cases} M_\mathrm{d}[f] = -H_i(s)(I_{\mathrm{rd}}[f] - I_\mathrm{d}[f]) - K_\mathrm{d}I_\mathrm{q}[f], \\ \qquad\qquad\qquad\qquad\qquad\qquad f = \pm(f_\mathrm{p} - f_1) \\ M_\mathrm{q}[f] = -H_i(s)I_\mathrm{q}[f] + K_\mathrm{d}I_\mathrm{d}[f], \quad f = \pm(f_\mathrm{p} - f_1) \end{cases} \tag{15}$$

where $H_i(s)$ is the transfer function of the current control, and $K_\mathrm{d}$ is the decoupling gain.

Then, the dq axis modulating signals are transformed to the abc frame through the reverse Park transformation. The modulated signal $M_\mathrm{a}[f]$ for phase A can be found as follows:

$$M_\mathrm{a}[f] = \begin{cases} F_{\mathrm{ip}}I_\mathrm{p} + F_{\mathrm{vp}}V_\mathrm{p}, & f = \pm f_\mathrm{p} \\ F_{\mathrm{ic}}I_\mathrm{p} + F_{\mathrm{vc}}V_\mathrm{p}, & f = \pm(f_\mathrm{p} - 2f_1) \end{cases} \tag{16}$$

Definitions for parameters in (16) can be found in Appendix (A1)–(A4).

*4) Modeling of Output Impedance and Frequency Coupling*

Since the fluctuation of the DC bus voltage exists in inverters, the phase-A terminal voltage can be written as follows:

$$Z_\mathrm{L}i_\mathrm{a} = K_\mathrm{m}v_\mathrm{dc} \otimes m_\mathrm{a} - v_\mathrm{a} \tag{17}$$

where $Z_\mathrm{L}$ is the impedance of filter inductance $L_\mathrm{p}$.

Combining (9), (16), and (17), the output impedance model and frequency coupling model can be obtained as follows:

$$Z_{\mathrm{pp}}(s) = \frac{I_{\mathrm{pp}} - H_{\mathrm{pp}}C_\mathrm{i}}{1 - T_{\mathrm{pp}} - H_{\mathrm{pp}}C_\mathrm{v}} \tag{18}$$

$$Z_{\mathrm{pn}}(s) = \frac{I_{\mathrm{pn}} - H_{\mathrm{pn}}C_\mathrm{i}}{-T_{\mathrm{pn}} - H_{\mathrm{pn}}C_\mathrm{v}} \tag{19}$$

In (18) and (19), some variables and parameters can be found in Appendix (A5)–(A7).

### C. Effect of Frequency Coupled Cross Term

Since frequency coupling exists in inverters, the model in (18) is a single input multiple output system; its stability analysis should be analyzed by using the generalized Nyquist criterion, which, conventionally, will not be helpful for identification of potential resonance points. Recently, a new method shows that the effects of frequency coupling characteristics can be considered just by paralleling additional impedance [25], and the impedance-based Nyquist criterion [15] can be used for analysis.

The output impedance of PVs with an ideal grid is given by (18). However, in a nonideal grid, the perturbation voltage with frequency $f_\mathrm{p}$ will also lead to a frequency coupling current response at frequency $f_\mathrm{p} - 2f_1$ according to (19). The frequency coupling current can be written as follows:

$$i_{\mathrm{pn}}(s - \mathrm{j}2\pi\omega_1) = -Y_{\mathrm{pn}}(s)v_\mathrm{p}(s) \tag{20}$$

The inverter-grid system can be represented by using the circuit diagram shown in Fig. 4.

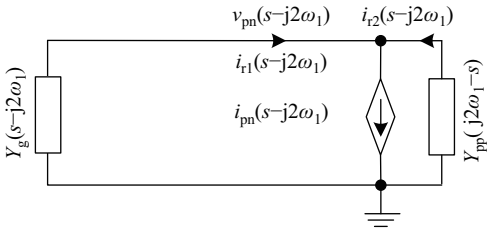


Fig. 4. Equivalent circuit of frequency-coupled response considering grid impedance.

In Fig. 4, $Y_\mathrm{g}(s-\mathrm{j}2\omega_1)$ is the grid admittance, $Y_{\mathrm{pp}}(\mathrm{j}2\omega_1 - s)$ is the output admittance of the inverter, $i_{\mathrm{pn}}(s - \mathrm{j}2\omega_1)$ is the frequency-coupled current, and $i_{\mathrm{r1}}(s-\mathrm{j}2\omega_1)$ and $i_{\mathrm{r2}}(s-\mathrm{j}2\omega_1)$ are the currents flowing through the grid admittance and the output admittance of the inverter, respectively.

Since the transformer is a passive device, its impedance can be equivalently regarded as part of the grid impedance in Fig. 1. The impedances of the primary side, the secondary side, and the entire transformer are shown in (21)–(23), respectively:

$$Z_1 = sL_1 + R_1 \tag{21}$$

$$Z_2 = sL_2 + R_2 \tag{22}$$

$$Z_\mathrm{b} = sL_\mathrm{b} + R_\mathrm{b} = \frac{Z_1}{n^2} + Z_2 \tag{23}$$

where $Z_1$, $Z_2$, and $Z_\mathrm{b}$ are the primary side impedance, secondary side impedance, and equivalent impedance of the transformer, respectively; $R_1$ and $L_1$ are the primary side resistance and inductance, $R_2$ and $L_2$ are the secondary side resistance and inductance, $R_\mathrm{b}$ and $L_\mathrm{b}$ are equivalent resistance and inductance of the transformer, respectively; and $n$ is winding turns ratio. Thus, the equivalent grid impedance $Z_\mathrm{g}$

(with the corresponding grid inductance denoted as $L_{\rm g}$) at PCC includes $Z_{\rm b}$ and $Z_0$. The equivalent grid admittance is:

$$Y_{\rm g} = \frac{1}{Z_{\rm g}} = \frac{1}{Z_{\rm b} + Z_0} \tag{24}$$

From Fig. 4, the frequency-coupled current response acts against the parallel impedances of the grid and the inverter to motivate a secondary voltage perturbation at the PCC.

$$v_{\rm pn}(s - {\rm j}2\pi\omega_1) = \frac{i_{\rm pn}(s - {\rm j}2\pi\omega_1)}{Y_{\rm g}(s - {\rm j}2\pi\omega_1) + Y_{\rm pp}({\rm j}2\pi\omega_1 - s)} \tag{25}$$

The secondary voltage induces a current that returns to the original perturbation frequency. This current can be written as follows:

$$i_{\rm pn2}(s) = Y_{\rm pn}(s - {\rm j}2\pi\omega_1)\frac{-Y_{\rm pn}(s)v_{\rm p}(s)}{Y_{\rm g}(s - {\rm j}2\pi\omega_1) + Y_{\rm pp}({\rm j}2\pi\omega_1 - s)} \tag{26}$$

The relationships between the current response generated by the perturbation voltages $v_{\rm p}(s)$ and $v_{\rm pn}(s - {\rm j}2\omega_1)$ can be shown in Fig. 5. $Y_{\rm pp}(s)$ is the admittance of the inverter, and $Y_{\rm pn}(s)$ is the cross-coupling frequency term. In (26), the cross-coupling frequency term $Y_{\rm pn2}(s)$ is defined as the ratio of $-i_{\rm pn}(s - {\rm j}2\omega_1)$ to $v_{\rm p}(s)$, and the relationships between the cross-coupling frequency term and the inverter output impedance is shown in Fig. 6. Then, the positive sequence equivalent output impedance with frequency coupling for inverter-grid systems can be obtained by (27). In the same way, the negative sequence equivalent output impedance of converter-grid system considering the coupling cross-term also can be obtained using (7).

$$Z_{\rm p}(s) = [Y_{\rm pp}(s) + Y_{\rm pn2}(s)]^{-1} \tag{27}$$

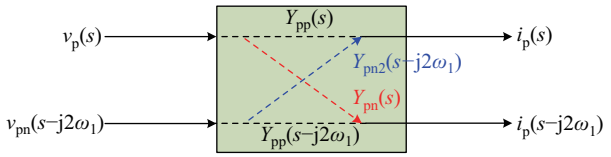


Fig. 5. Current responses caused by voltage perturbation and secondary voltage perturbation considering grid impedance.

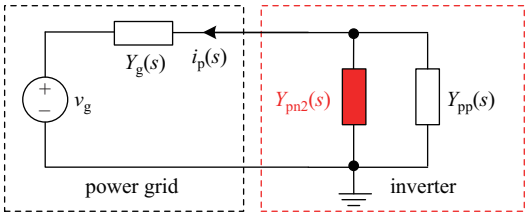


Fig. 6. Relationships between positive sequence output impedance and cross-coupling frequency term.

## IV. Case Analysis

A PV generation system with the capacity of 1 MW is taken as an example to verify the advantages of the impedance model considering frequency coupling. First, the time domain simulation model is built in MATLAB/Simulink, and the hardware-in-the-loop experiments are carried out in RT-Lab. The detailed parameters of the model are shown in Table II. Secondly, a small-signal impedance model considering frequency coupling is developed by harmonic linearization, and the curves of the positive/negative sequence impedance and frequency-coupled characteristics of the PV generation system are analyzed. Finally, the effects of different grid impedance, DC bus capacitance and DC voltage control on the coupling characteristics and stability of a grid-connected photovoltaic inverter are studied.

### A. Output Impedance and Frequency-coupled Curves of PVs

The expressions of the inverter output impedance and the frequency coupled under positive and negative sequence voltage perturbation are shown in (18) and (19). It only accounts for the frequency coupling effects in the inverter. Similarly, according to the relationships between the positive and negative sequence impedance in (7), the expressions of the inverter output impedance $Z_{\rm nn}$ and frequency coupled $Z_{\rm np}$ under negative sequence voltage perturbation can be obtained. According to the main circuit parameters and PI controller parameters in Table II, curves of the positive/negative sequence inverter output impedance and frequency coupled can be drawn as in Fig. 7.

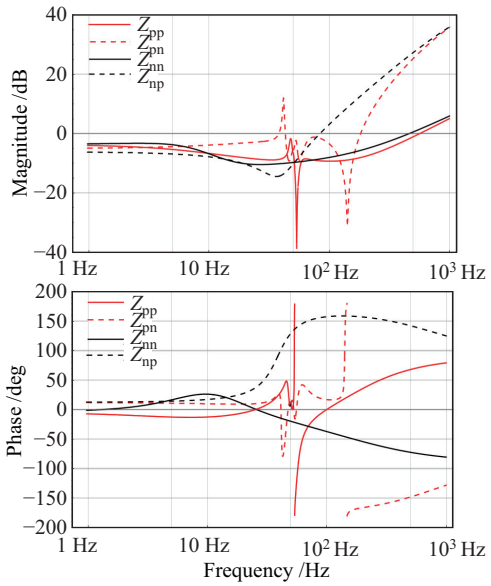


Fig. 7. Positive/negative sequence output impedance and frequency coupling ($Z_{\rm pp}$ and $Z_{\rm pn}$ are the output impedance and frequency coupling terms of positive sequence perturbation, respectively. $Z_{\rm nn}$ and $Z_{\rm np}$ are the output impedance and frequency coupling terms of negative sequence perturbation respectively).

Compared with the curve in Fig. 7, the amplitude of the inverter impedance in the middle and low frequency band is close to the amplitude of the frequency-coupled term, but in the high frequency band, the frequency-coupled amplitude is much larger than the impedance amplitude of the inverter, so the impact of frequency coupling on the impedance of the inverter is primarily concentrated in the middle and low frequency band.

TABLE II
SIMULATION PARAMETERS OF PVS

| Parameter | Symbol | Value | Parameter | Symbol | Value |
|---|---|---|---|---|---|
| Rated power | $S$ | 1 MW | MPPT control proportional gain | $K_{\mathrm{mp}}$ | 3 |
| DC bus voltage | $V_{\mathrm{rd0}}$ | 1150 V | MPPT control integral gain | $K_{\mathrm{mi}}$ | 173 |
| DC capacitor | $C_{\mathrm{dc}}$ | 10 mF | Modulation gain | $K_{\mathrm{m}}$ | $8.69 \times 10^{-4}$ |
| Filter inductor | $L_{\mathrm{p}}$ | 0.35 mH | Grid inductor | $L_{\mathrm{g}}$ | 0.083 mH |
| DC control proportional gain | $K_{\mathrm{vp}}$ | 1 | Transformer primary voltage | $V_1$ | 33 kV |
| DC control integral gain | $K_{\mathrm{vi}}$ | 5 | Transformer primary resistance | $R_1$ | 13.06 Ω |
| Current control proportional gain | $K_{\mathrm{ip}}$ | 0.33 | Transformer primary inductor | $L_1$ | 0.3 H |
| Current control integral gain | $K_{\mathrm{ii}}$ | 20 | Transformer secondary voltage | $V_2$ | 690 V |
| PLL control proportional gain | $K_{\mathrm{pp}}$ | 60 | Transformer secondary resistance | $R_2$ | $1.9 \times 10^{-3}$ Ω |
| PLL control integral gain | $K_{\mathrm{pi}}$ | 1400 | Transformer secondary inductor | $L_2$ | 0.045 mH |

When the grid impedance cannot be neglected, especially when the inverter is connected to a weak AC grid, the impact of the cross-coupling term on the inverter output impedance should be considered. When $L_{\mathrm{g}}$ at PCC is set to 0.75 mH (short-circuit ratio, SCR = 2), curves of the inverter output impedance with/without considering cross-coupling term and cross-coupling term can be obtained based on (27), as shown in Fig. 8.

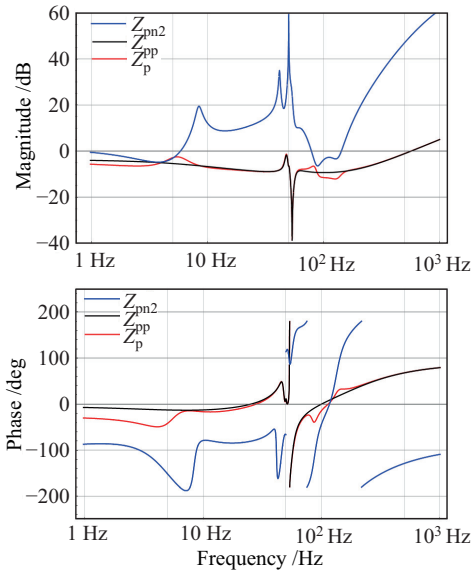


Fig. 8. Curves of output impedance of inverter with/without considering coupling effects between inverter and grid ($Z_{\mathrm{pn2}}$ is the cross-coupling term. $Z_{\mathrm{p}}/Z_{\mathrm{pp}}$ is the impedance with/without considering the grid-coupling term).

In order to test the impacts of the cross-coupling frequency term on equivalent output impedance under different conditions of grid impedances, the equivalent output impedance curves of the inverter which considers cross-coupling terms when $L_{\mathrm{g}} = 0.75$ mH (SCR = 2), $L_{\mathrm{g}} = 0.377$ mH (SCR = 4), $L_{\mathrm{g}} = 0.075$ mH (SCR = 20) are plotted in Fig. 9. It can be seen that the higher the grid impedance is, the stronger the impact exists on the inverter output impedance.

### B. Stability Analysis of PVs

#### 1) Stability Analysis of Sequential Impedance Model Considering Frequency Coupling

It is assumed that the grid impedance ($L_{\mathrm{g}} = 0.083$ mH, SCR = 20) exists, and the parameters of PVs are listed in Table II. Based on (27), the inverter output impedance which

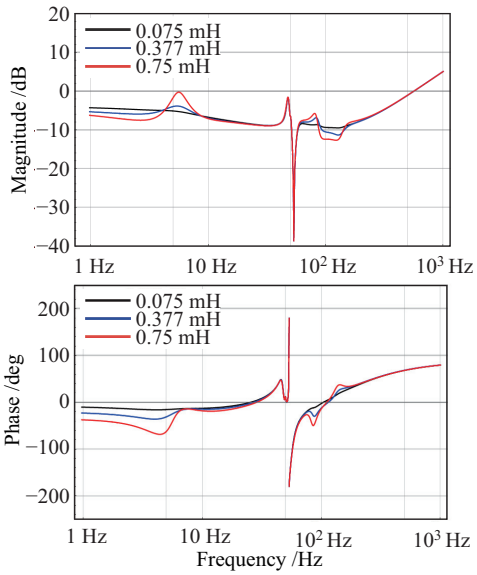


Fig. 9. Output impedance of inverter considering the cross-coupling term under different grid impedances.

considers the frequency coupling and the grid impedance can be obtained, as shown in Fig. 10. The 1/1150 per-unit value three-phase currents at PCC and the DC bus voltage are shown in Fig. 11 respectively. Their THD at PCC is shown in Fig. 12.

From Fig. 10, it can be observed that when the cross-coupling term is considered, there is no intersection between the output impedance curve of the inverter and the grid impedance curve in the low frequency band. The time domain simulation result shows that the waveform of the three-phase currents is not significantly distorted, and no oscillation occurs. The THD analysis of the three phase grid-connected currents in Fig. 12 also demonstrates that there is no resonance point in the low frequency band.

When the grid impedance increases to $L_{\mathrm{g}} = 0.75$ mH (SCR = 2), the output impedance curve of the inverter with frequency coupling, and the grid impedance curve are shown in Fig. 13. The 1/1150 per-unit value three-phase currents at PCC and the DC bus voltage are shown in Fig. 14 respectively. Their THD at PCC is shown in Fig. 15.

From Fig. 14, it can be seen that oscillation occurs. As shown in Fig. 15, the two frequencies with the highest harmonic magnitudes are 43 Hz and 57 Hz, respectively. They are located symmetrically on both sides of the fundamental frequency (50 Hz), and 43 Hz is the mirror frequency for

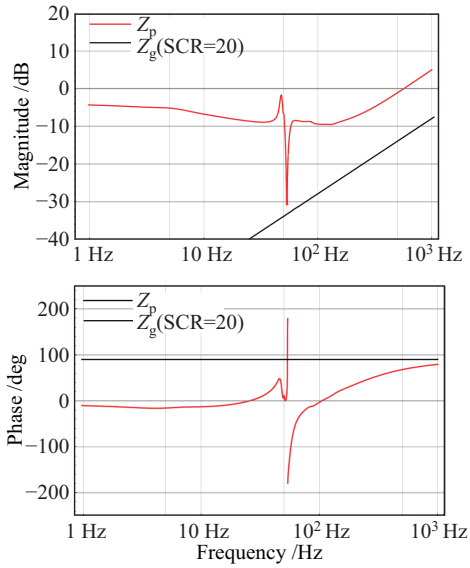


Fig. 10. Output impedance curve considering cross-coupling term and line impedance curve under $L_g = 0.083$ mH (SCR=20).

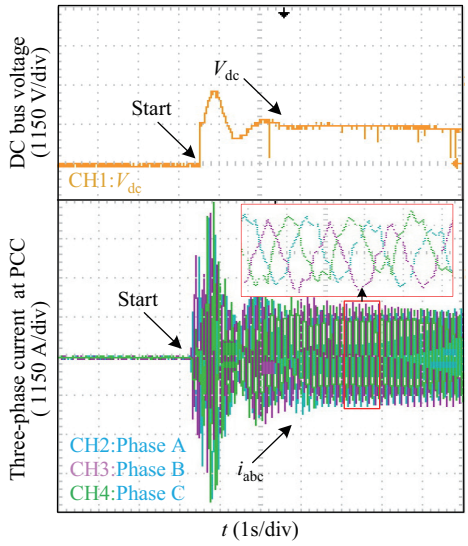


Fig. 11. Experimental waveforms of three-phase current and DC bus voltage at PCC under $L_g = 0.083$ mH (SCR = 20).

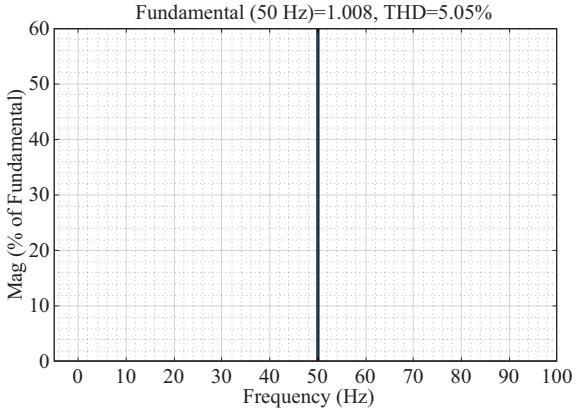


Fig. 12. THD of PCC current with $L_g = 0.3769$ mH (SCR = 4).

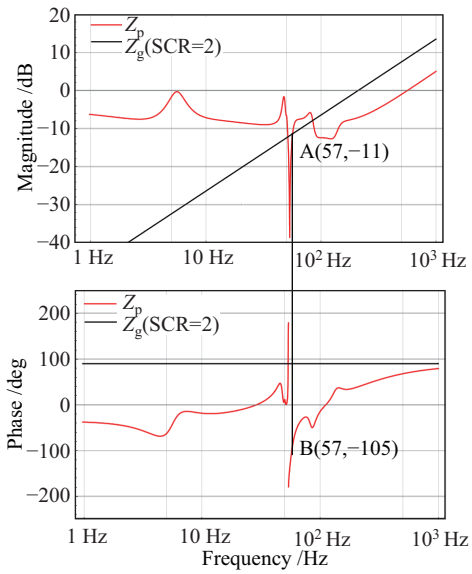


Fig. 13. Output impedance curve considering cross-coupling term and line impedance curve under $L_g = 0.75$ mH (SCR = 2).

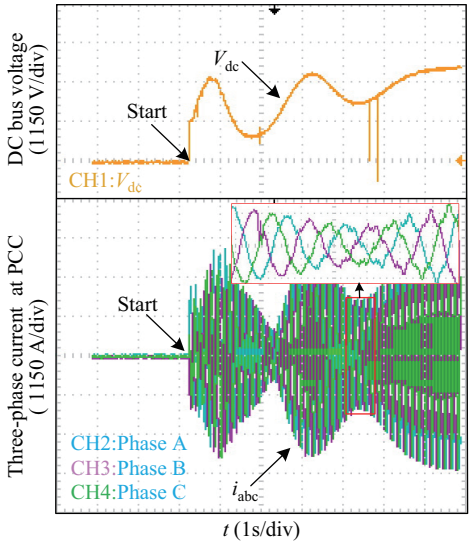


Fig. 14. Experimental waveforms of three-phase current and DC bus voltage at PCC under $L_g$ =0.75 mH (SCR = 2).

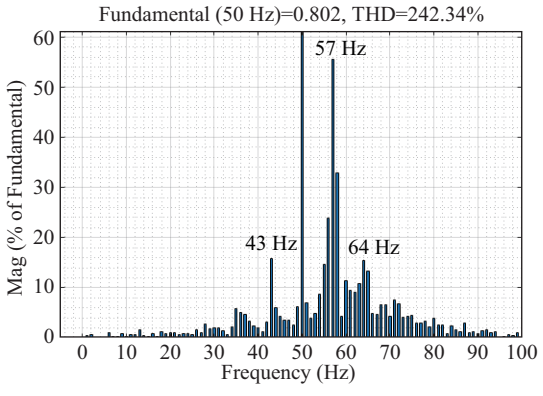


Fig. 15. THD of PCC current under $L_g$ =0.75 mH (SCR = 2).

57 Hz. The frequency of 57 Hz is exactly equal to the frequency at the intersection point A between the inverter output impedance and grid impedance in Fig. 13. The phase of the output impedance at 57 Hz is flipped from positive 180 degrees to negative 105 degrees, the PVs creates resonance and becomes unstable, and 43 Hz is the coupled resonance point. In addition, there is another frequency with the higher harmonic magnitudes at 64 Hz in Fig. 15, which is the intersection point between the negative sequence inverter output impedance and grid impedance. The analysis method is similar to the positive order, which will not be discussed here.

*2) Stability Comparison and Simulation of PVs*

When the effect of the DC voltage control is neglected, the output impedance model of the inverter which considers frequency coupling, as shown in (18), can be simplified as follows:

$$Z^1_{\rm pp}(s) = \frac{I_{\rm pp}}{1 - T_{\rm pp}} \tag{28}$$

Assuming that the grid impedance is still set to $L_{\rm g} = 0.75$ mH (SCR $= 2$), the output impedance without considering frequency coupling is obtained according to (28), and the curves of the grid impedance and the output impedance without considering frequency coupling are shown in Fig. 16.

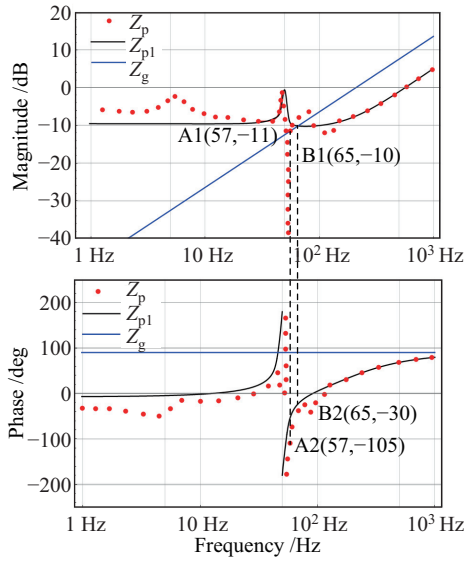


Fig. 16. Curves of output impedance with/without considering frequency coupling and line impedance.

From Fig. 16, it is seen that the output impedance curve without considering frequency coupling intersects with the grid

impedance curve at 65 Hz. However, the THD in Fig. 15 shows that there are two positive sequence resonance points in the low frequency band at the frequencies of 43 Hz and 57 Hz. The results of stability analysis of the impedance model are inconsistent with the analysis in the time domain simulation. Comparing Fig. 15 and Fig. 16, the conclusion can be drawn that the impedance model of the PVs considering frequency coupling is more effective, and predicts the potential resonance point of the system more accurately.

### *C. Effects of DC Bus Voltage Control Loop on Frequency Coupling Characteristics*

In (18) and (19), the output impedance model of the inverter and frequency coupling are given, which considers many factors such as the PLL control, DC bus capacitance, and DC voltage control with MPPT. In order to analyze the effects of the DC bus voltage control on frequency coupling of the PVs separately, it is necessary to simplify the models in (18) and (19), ignoring the effect of the PLL bandwidth on frequency coupling. The simplified model is shown as follows:

$$Z^2_{\rm pp}(s) = \frac{I_{\rm pp} - F_{\rm pp}C_{\rm ip}}{1 - F_{\rm pp}C_{\rm vp}} \tag{29}$$

$$Z^2_{\rm pn}(s) = \frac{I_{\rm pn} - F_{\rm pn}C_{\rm ip}}{-F_{\rm pn}C_{\rm vp}} \tag{30}$$

The impact of the DC bus voltage control on frequency coupling has two aspects: one is the size of DC bus capacitance; the other is the bandwidth of the DC bus voltage controller with MPPT. The frequency coupling curves under DC capacitors with different sizes and different bandwidths of DC voltage controllers are shown in Fig. 17 and Fig. 18 respectively.

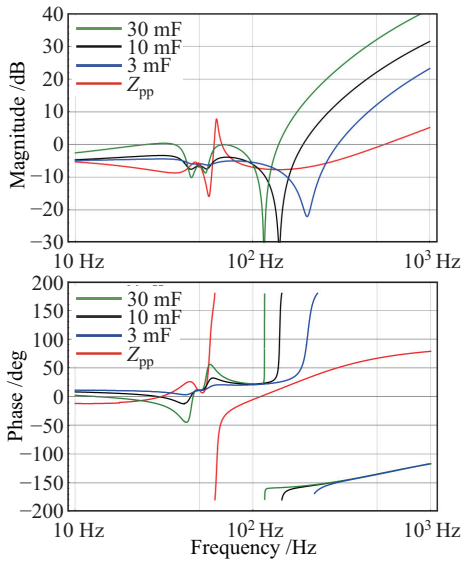


Fig. 17. Frequency coupling curves of different DC capacitors and output impedance curve of inverter.

Figure 17 shows that when the DC bus capacitance is smaller, the frequency coupling is closer to the inverter output impedance, and the effect on the inverter output impedance is greater in the high frequency section. The function of the DC bus capacitor is to stabilize the DC side voltage. When the capacitor is larger, the DC side voltage is more stable. This phenomenon coincides with the curves in Fig. 17.

Effects under different bandwidths of the DC bus voltage controller with MPPT are shown in Fig. 18. When the bandwidth of the DC bus voltage controller is narrower, the difference between the amplitudes of the frequency coupling and the output impedance becomes larger, and the impact on the impedance of the inverter becomes smaller in the high frequency section. When the bandwidth of the PI controller

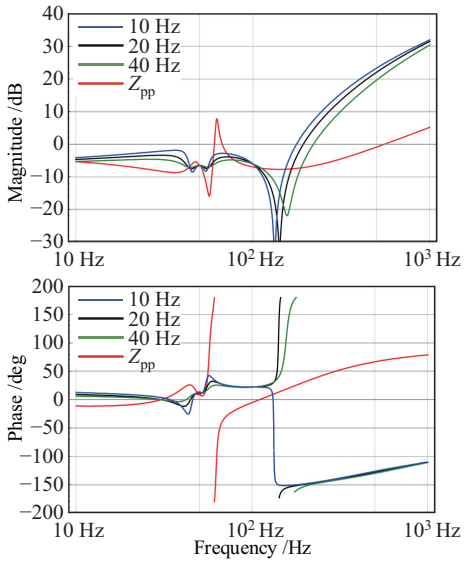


Fig. 18. Frequency coupling curves of bandwidth of different DC voltage controllers and output impedance curve of inverter.

is larger, the response speed of the system stability is faster, but it becomes more unstable at the same time. This fact also confirms the curves plotted in Fig. 18.

## V. Conclusion

This paper focuses on the mechanism of frequency coupling in the DC bus voltage control of grid-connected photovoltaic inverters. The sequence impedance model of grid-connected photovoltaic inverters considering frequency coupling is developed. The impacts of the DC bus voltage control on frequency coupling are quantitatively analyzed. The main conclusions of this paper are as follows:

1) Compared to conventional models, the sequence impedance model of PVs considering frequency coupling is more accurate, which based on the resonance point of sub-synchronous oscillation can be predicted more accurately.

2) When the grid-connected photovoltaic inverter is connected to a weak AC grid through coupling transformers, the equivalent grid impedance at PCC is higher, which increases the degree of frequency coupling, and the impact on the inverter output impedance becomes greater.

3) Whenthe DC bus capacitance of the grid-connected photovoltaic inverter is smaller, or the bandwidth of the DC bus controller with MPPT is wider, the degree of frequency coupling will become higher, which will increase the risk of SSO occurrence in the system.

## Appendix

$$\begin{bmatrix} F_{\mathrm{ip}}(\mathrm{j}2\pi(f_{\mathrm{p}}-f_1)) \\ F_{\mathrm{ic}}(\mathrm{j}2\pi(f_{\mathrm{p}}-f_1)) \end{bmatrix} = \begin{bmatrix} H_i(s)H_{\mathrm{v}}(s)(H_{\mathrm{m}}(s)-1)C_{\mathrm{i}} \\ -[H_{\mathrm{i}}(s)-\mathrm{j}K_{\mathrm{d}}] \\ H_{\mathrm{i}}(s)H_{\mathrm{v}}(s)(H_{\mathrm{m}}(s)-1)C_{\mathrm{i}} \end{bmatrix} \tag{A1}$$

$$\begin{bmatrix} F_{\mathrm{vp}}(\mathrm{j}2\pi(f_{\mathrm{p}}-f_1)) \\ F_{\mathrm{vc}}(\mathrm{j}2\pi(f_{\mathrm{p}}-f_1)) \end{bmatrix} = \begin{bmatrix} \frac{1}{2}\left\{ \begin{array}{c} [(H_{\mathrm{i}}(s)-\mathrm{j}K_{\mathrm{d}})I_1+M_1]G_{\mathrm{p}}(s) \\ +H_i(s)H_{\mathrm{v}}(s)(H_{\mathrm{m}}(s)-1)C_{\mathrm{v}} \end{array} \right\} \\ -\frac{1}{2}\left\{ \begin{array}{c} [(H_{\mathrm{i}}(s)+\mathrm{j}K_{\mathrm{d}})I_1^*+M_1^*]G_{\mathrm{p}}(s) \\ +H_i(s)H_{\mathrm{v}}(s)(H_{\mathrm{m}}(s)-1)C_{\mathrm{v}} \end{array} \right\} \end{bmatrix} \tag{A2}$$

$$\begin{bmatrix} C_{\mathrm{i}} \\ C_{\mathrm{v}} \end{bmatrix} = \begin{bmatrix} \frac{3(sL_{\mathrm{p}}I_1^*+V_1)}{2(I_{\mathrm{dc}}-sC_{\mathrm{dc}}V_{\mathrm{rd0}})} \\ \frac{3I_1^*}{2(I_{\mathrm{dc}}-sC_{\mathrm{dc}}V_{\mathrm{rd0}})} \end{bmatrix} \tag{A3}$$

$$M_1 = \frac{V_1+\mathrm{j}2\pi f_1 L_{\mathrm{p}} I_1}{K_{\mathrm{m}}V_{\mathrm{rd0}}} \tag{A4}$$

where $M_1$ is the modulated signal in steady state, and $M_1^*$ is the conjugate of $M_1$.

$$\begin{bmatrix} I_{\mathrm{pp}} \\ I_{\mathrm{pn}} \end{bmatrix} = \begin{bmatrix} K_{\mathrm{m}}V_{\mathrm{rdc}}[H_{\mathrm{i}}(s-\mathrm{j}2\pi f_1)-\mathrm{j}K_{\mathrm{d}}]+sL_{\mathrm{p}}+R_{\mathrm{b}} \\ (s-\mathrm{j}4\pi f_1)L_{\mathrm{p}} \end{bmatrix} \tag{A5}$$

$$\begin{bmatrix} H_{\mathrm{pp}} \\ H_{\mathrm{pn}} \end{bmatrix} = \begin{bmatrix} \frac{1}{2}[K_{\mathrm{m}}V_{\mathrm{rdc}}H_{\mathrm{v}}(s-\mathrm{j}2\pi f_1) \\ \times(H_{\mathrm{m}}(s-\mathrm{j}2\pi f_1)-1)H_{\mathrm{i}}(s-\mathrm{j}2\pi f_1)+K_{\mathrm{m}}M_1] \\ \frac{1}{2}[K_{\mathrm{m}}V_{\mathrm{rdc}}H_{\mathrm{v}}(s-\mathrm{j}2\pi f_1) \\ \times(H_{\mathrm{m}}(s-\mathrm{j}2\pi f_1)-1)H_{\mathrm{i}}(s-\mathrm{j}2\pi f_1)+K_{\mathrm{m}}M_1^*] \end{bmatrix} \tag{A6}$$

$$\begin{bmatrix} T_{\mathrm{pp}} \\ T_{\mathrm{pn}} \end{bmatrix} = \begin{bmatrix} \frac{1}{2}K_{\mathrm{m}}V_{\mathrm{rdc}}G_{\mathrm{p}}(s\mp\mathrm{j}2\pi f_1) \\ \times\{[H_{\mathrm{i}}(s-\mathrm{j}2\pi f_1)-\mathrm{j}K_{\mathrm{d}}]I_1+M_1\} \\ -\frac{1}{2}K_{\mathrm{m}}V_{\mathrm{rdc}}G_{\mathrm{p}}(s\pm\mathrm{j}2\pi f_1) \\ \times\{[H_{\mathrm{i}}(s-\mathrm{j}2\pi f_1)+\mathrm{j}K_{\mathrm{d}}]I_1^*+M_1^*\} \end{bmatrix} \tag{A7}$$

## References


[1] X. M. Yuan, S. J. Cheng, and J. B. Hu, "Multi-time scale voltage and power angle dynamics in power electronics dominated large power systems," *Proceedings of the CSEE*, vol. 36, no. 19, pp. 5145–5154, Oct. 2016.

[2] J. Sun, M. J. Li, Z. G. Zhang, T. Xu, J. B. He, H. J. Wang, and G. H. Li, "Renewable energy transmission by HVDC across the continent: system challenges and opportunities," *CSEE Journal of Power and Energy Systems*, vol. 3, no. 4, pp. 353–364, Dec. 2017.

[3] C. Q. Kang and L. Z. Yao, "Key scientific issues and theoretical research framework for power systems with high proportion of renewable energy," *Automation of Electric Power Systems*, vol. 41, no. 9, pp. 2–11, May 2017.

[4] X. R. Xie, H. K. Liu, J. B. He, H. Liu, and W. Liu, "On new oscillation issues of power systems," *Proceedings of the CSEE*, vol. 38, no. 10, pp. 2821–2828, May 2018.

[5] C. Chen, W. J. Du, H. F. Wang, and T. Littler, "Sub-synchronous oscillations in power systems caused by grid-connected wind farms—A survey of mechanism studies," *CSEE Journal of Power and Energy Systems*, vol. 4, no. 4, pp. 495–503, Dec. 2018.

[6] W. S. Wang, C. Zhang, G. Q. He, G. H. Li, J. Y. Zhang, and H. J. Wang, "Overview of research on subsynchronous oscillations in large-scale wind farm integrated system," *Power System Technology*, vol. 41, no. 4, pp. 1050–1060, Apr. 2017.

[7] Y. Y. Xu, H. Nian, T. Wang, L. Chen, and T. Y. Zheng, "Frequency coupling characteristic modeling and stability analysis of doubly fed induction generator," *IEEE Transactions on Energy Conversion*, vol. 33, no. 3, pp. 1475–1486, Sep. 2018.

[8] B. F. Gao, J. Liu, R. Li, and S. Q. Zhao, "Studies of sub-synchronous control interaction in wind turbine generators," *Transactions of China Electrotechnical Society*, vol. 30, no. 16, pp. 154–161, Aug. 2015.

[9] Y. F. Dong, Y. L. Wang, J. Han, Y. W. Li, S. H. Miao, and J. X. Hou, "Review of high efficiency digital electromagnetic transient simulation technology in power system," *Proceedings of the CSEE*, vol. 38, no. 8, pp. 2213–2231, Apr. 2018.

[10] Q. Fu, W. J. Du, and H. F. Wang, "Small signal stability analysis of AC/DC hybrid power system: an overview," *Proceedings of the CSEE*, vol. 38, no. 10, pp. 2829–2840, May 2018.
[11] X. Z. Xi, H. Geng, and G. Yang, "Enhanced model of the doubly fed induction generator-based wind farm for small-signal stability studies of weak power system," *IET Renewable Power Generation*, vol. 8, no. 7, pp. 765–774, Sep. 2014.
[12] P. H. Huang, M. S. El Moursi, W. D. Xiao, and J. L Kirtley, "Subsynchronous resonance mitigation for series-compensated DFIG-based wind farm by using two-degree-of-freedom control strategy," *IEEE Transactions on Power Systems*, vol. 30, no. 3, pp. 1442–1454, May 2015.
[13] M. Cespedes and J. Sun, "impedance modeling and analysis of grid-connected voltage-source converters," *IEEE Transactions on Power Electronics*, vol. 29, no. 3, pp. 1254–1261, Mar. 2014.
[14] J. Sun, "Small-signal methods for ac distributed power systems–A review," *IEEE Transactions on Power Electronics*, vol. 24, no. 11, pp. 2545–2554, Nov. 2009.
[15] J. Sun, "Impedance-based stability criterion for grid-connected inverters," *IEEE Transactions on Power Electronics*, vol. 26, no. 11, pp. 3075–3078, Nov. 2011.
[16] J. Sun and H. C. Liu, "Sequence impedance modeling of modular multilevel converters," *IEEE Journal of Emerging and Selected Topics in Power Electronics*, vol. 5, no. 4, pp. 1427–1443, Dec. 2017.
[17] I. Vieto and J. Sun, "Sequence impedance modeling and analysis of type-III wind turbines," *IEEE Transactions on Energy Conversion*, vol. 33, no. 2, pp. 537–545, Jun. 2018.
[18] X. F. Wang and F. Blaabjerg, "Harmonic stability in power electronic-based power systems: concept, modeling, and analysis," *IEEE Transactions on Smart Grid*, vol. 10, no. 3, pp. 2858–2870, May 2019.
[19] Y. C. Wang, X. Chen, J. Chen, and C. Y. Gong, "Analysis of positive-sequence and negative-sequence impedance modeling of three-phase LCL-type grid-connected inverters based on harmonic linearization," *Proceedings of the CSEE*, vol. 36, no. 21, pp. 5890–5898, Nov. 2016.
[20] S. Shah and L. Parsa, "Impedance modeling of three-phase voltage source converters in DQ, sequence, and phasor domains," *IEEE Transactions on Energy Conversion*, vol. 32, no. 3, pp. 1139–1150, Sep. 2017.
[21] H. Nian, Y. Y. Xu, L. Chen, and G. H. Li, "Frequency coupling characteristic modeling of grid-connected inverter and system stability analysis," *Proceedings of the CSEE*, vol. 39, no. 5, pp. 1421–1431, Mar. 2019.
[22] X. M. Zou, X. Du, G. N. Wang, Y. G. Yang, and Y. L. Ji, "Frequency coupling mechanism analysis and stability judgement for three-phase grid-connected inverter," *Automation of Electric Power Systems*, vol. 42, no. 18, pp. 57–63, Sep. 2018.
[23] C. Zhang, X. Cai, A. Rygg, and M. Molinas, "Sequence domain SISO equivalent models of a grid-tied voltage source converter system for small-signal stability analysis," *IEEE Transactions on Energy Conversion*, vol. 33, no. 2, pp. 741–749, Jun. 2018.
[24] J. Sun, G. N. Wang, X. Du, and H. J. Wang, "A theory for harmonics created by resonance in converter-grid systems," *IEEE Transactions on Power Electronics*, vol. 34, no. 4, pp. 3025–3029, Apr. 2019.
[25] I. Vieto and J. Sun, "Sequence impedance modeling and converter-grid resonance analysis considering DC bus dynamics and mirrored harmonics," in *Proceedings of 2018 IEEE 19th Workshop on Control and Modeling for Power Electronics*, Padua, Italy, 2018, pp. 1–8.
[26] S. Q. Zhao, R. Li, B. F. Gao, N. Wang, and X. Zhang, "Subsynchronous oscillation of PV plants integrated to weak AC networks," *IET Renewable Power Generation*, vol. 13, no. 3, pp. 409–417, Feb. 2019.
[27] I. Vieto, G. H. Li, and J. Sun, "Behavior, modeling and damping of a new type of resonance involving type-III wind turbines," in *Proceedings of 2018 IEEE 19th Workshop on Control and Modeling for Power Electronics*, Padua, Italy, 2018, pp. 1–8.
[28] Y. Y. Xu, H. Nian, G. D. Xu, and J. X. Qiu, "Cross-coupling over frequency and sequence in impedance modelling of grid-connected inverter," *The Journal of Engineering*, vol. 2017, no. 13, pp. 990–995, Nov. 2017.
[29] X. F. Wang, L. Harnefors, and F. Blaabjerg, "Unified impedance model of grid-connected voltage-source converters," *IEEE Transactions on Power Electronics*, vol. 33, no. 2, pp. 1775–1787, Feb. 2018.
[30] A. Rygg, M. Molinas, C. Zhang, and X. Cai, "A modified sequence-domain impedance definition and its equivalence to the dq-domain impedance definition for the stability analysis of ac power electronic systems," *IEEE Journal of Emerging and Selected Topics in Power Electronics*, vol. 4, no. 4, pp. 1383–1396, Dec. 2016.
[31] M. K. Bakhshizadeh, X. F. Wang, F. Blaabjerg, J. Hjerrild, Ł. Kocewiak, C. L. Bak, and B. Hesselbæk, "Couplings in phase domain impedance modeling of grid-connected converters," *IEEE Transactions on Power Electronics*, vol. 31, no. 10, pp. 6792–6796, Oct. 2016.
[32] M. Dong and A. Luo, "Design and control strategies of inverters for a grid-connected photovoltaic power system," *Automation of Electric Power Systems*, vol. 30, no. 20, pp. 97–102, Oct. 2006.
[33] C. Wu, H. Nian, B. Pang, and P. Cheng, "Adaptive repetitive control of DFIG-DC system considering stator frequency variation," *IEEE Transactions on Power Electronics*, vol. 34, no. 4, pp. 3302–3312, Apr. 2019.
[34] H. T. Wu, Y. H. Liu, and Z. H. Wang, "Implementation of a new high-power current-source single-stage PV grid-connected system with reactive power compensation," *IET Renewable Power Generation*, vol. 13, no. 11, pp. 1873–1881, Aug. 2019.
[35] Y. Zhang, X. Chen, and J. Sun, "Impedance modeling and analysis of MMC in single-star configuration," in *Proceedings of 2017 IEEE 18th Workshop on Control and Modeling for Power Electronics*, Stanford, CA, USA, 2017, pp. 1–8.
[36] W. Ren and E. Larsen, "A refined frequency scan approach to sub-synchronous control interaction (SSCI) study of wind farms," *IEEE Transactions on Power Systems*, vol. 31, no. 5, pp. 3904–3912, Sep. 2016.
[37] A. K. Podder, N. K. Roy, and H. R. Pota, "MPPT methods for solar PV systems: a critical review based on tracking nature," *IET Renewable Power Generation*, vol. 13, no. 10, pp. 1615–1632, Jul. 2019.
[38] Y. B. Shu, X. X. Zhou, and W. F. Li, "Analysis of low frequency oscillation and source location in power systems," *CSEE Journal of Power and Energy Systems*, vol. 4, no. 1, pp. 5866, Mar. 2018.
[39] C. Chen, W. J. Du, H. F. Wang and T. Littler, "Sub-synchronous oscillations in power systems caused by grid-connected wind farms A survey of mechanism studies," *CSEE Journal of Power and Energy Systems*, vol. 4, no. 4, pp. 495–503, Dec. 2018.
[40] Y. N. Chi, B. J. Tang, J. B. Hu, X. S. Tian, H. Y. Tang, Y. Li, S. J. Sun, L. Shi, and L. Shuai, "Overview of mechanism and mitigation measures on multi-frequency oscillation caused by large-scale integration of wind power," *CSEE Journal of Power and Energy Systems*, vol. 5, no. 4, pp. 433–443, Dec. 2019.
[41] J. Ma, D. W. Zhao, L. Z. Yao, M. H. Qian, K. Yamashita, and L. Z. Zhu, "Analysis on application of a current-source based DFIG wind generator model," *CSEE Journal of Power and Energy Systems*, vol. 4, no. 3, pp. 352361, Sep. 2018.

**Shaojian Song** (M'18) received his B.S. degree in Industrial Electrical Automation, and M.S. degree in Control Science and Engineering from Guangxi University, Nanning, China, in 1994 and 2001 respectively. Since 1994, he has been with the school of Electrical Engineering at Guangxi University, where he became a Professor in 2010. He attended the New York State Center for Future Energy Systems at Rensselaer Polytechnic Institute, USA, from 2014 to 2015. His current research interests include power electronics and energy conversion, active distribution networks, state estimation, optimal control and machine learning.

**Ze Wei** received his B.S. degree in Measurement and Control Technology and Instrument from Changsha University of Technology, Changsha, China, in 2017. He is currently pursuing the M.Sc. degree at the school of Electrical Engineering, Guangxi University. His main research direction is the conversion and control of new energy sources.

**Yuzhang Lin** (M'18) is currently an assistant professor in the Department of Electrical and Computer Engineering at the University of Massachusetts, Lowell, MA, USA. He obtained his Bachelor and Master's degrees from Tsinghua University, Beijing, China, and Ph.D. degree from Northeastern University, Boston, MA, USA. His research interests include smart grid modeling, monitoring, data analytics, and cyber-physical security. He is a subject editor of the CSEE Journal of Power and Energy Systems.

**Bin Liu** received his Ph.D. degree from the School of Information Science and Engineering, Central South University, Changsha, China, in 2014.

He is currently a Lecturer in the School of Electrical Engineering, Guangxi University. His research interests are in the general area of power electronics and energy conversion, with particular emphasis on converter topologies, modeling, control, and various applications.

**Hui Liu** (M'12–SM'18) received his M.S. degree in 2004 and Ph.D. degree in 2007 from the School of Electrical Engineering at Guangxi University, Nanning, China, both in Electrical Engineering. He worked at Tsinghua University as a postdoctoral fellow from 2011 to 2013 and in Jiangsu University as a faculty member from 2007 to 2016. He attended the Energy Systems Division at Argonne National Laboratory, Argonne, IL, USA, from 2014 to 2015. He joined the School of Electrical Engineering at Guangxi University in 2016, where he is a professor. He is an Associate Editor of the IEEE Access and the IET Generation, Transmission & Distribution. He is also a reviewer for more than 20 journals. His research interests include power system optimization, power system stability and control, electric vehicles, integrated energy systems, and demand response, etc.